HR-GLDD: A globally distributed dataset using generalized DL for rapid landslide mapping on HR satellite imagery

Sansar Raj Meena [1], Lorenzo Nava [1], Kushanav Bhuyan [1], Silvia Puliero [1], Lucas Pedrosa Soares [2], Helen Cristina Dias [2], Mario Floris [1], Filippo Catani [1*]

1. Machine Intelligence and Slope Stability Laboratory, Department of Geosciences, University of Padova, 35129 Padua, Italy
2. Institute of Energy and Environment, University of São Paulo, São Paulo 05508-010, Brazil

* Correspondence: sansarraj.meena@unipd.it

Abstract:

Multiple landslide events occur often across the world which have the potential to cause significant harm to both human life and property. Although a substantial amount of research has been conducted to address mapping of landslides using Earth Observation (EO) data, several gaps and uncertainties remain when developing models to be operational at the global scale. The lack of a high resolution globally distributed and event-diverse dataset for landslide segmentation poses a challenge in developing machine learning models that can accurately and robustly detect landslides in various regions, as the limited representation of landslide and background classes can result in poor generalization performance of the models. To address this issue, we present the high-resolution global landslide detector database (HR-GLDD), a high resolution (HR) satellite dataset (PlanetScope, 3 m pixel resolution) for landslide mapping composed of landslide instances from ten different physiographical regions globally: South and South-East Asia, East Asia, South America, and Central America. The dataset contains five rainfall--triggered and five earthquake-triggered multiple landslide events that occurred in varying geomorphological and topographical regions in the form of standardized image patches containing four PlanetScope image bands (red, green, blue, and NIR) and a binary mask for landslide detection. The HRGLDD can be accessed through this link https://doi.org/10.5281/zenodo.7189381 (Meena et al., 2022a).. HR-GLDD is one of the first dataset for landslide detection generated by high resolution satellite imagery which can be useful for applications in artificial intelligence for landslide segmentation and detection studies. Five state of the art deep learning models were used to test the transferability and robustness of the HR-GLDD. Moreover, three three recent landslide events were used for testing the performance and usability of the dataset to comment on the detection of newly occurring significant landslide events. The deep learning models showed similar results for testing the HR-GLDD in individual test sites thereby indicating the robustness of the dataset for such purposes. The HR-GLDD can be accessed open access and it has the potential to calibrate and develop models to produce reliable inventories using high resolution satellite imagery after the occurrence of new significant landslide events. The HR-GLDD will be updated regularly by integrating data from new landslide events.

1. Introduction

With the increasing impacts of climate change, increased urbanization, and anthropogenic pressure in recent years, the risk from hazards to population, infrastructure, and essential life services has exacerbated. Landslides are quite ubiquitous and account for approximately 4.9% of all the natural disasters and 1.3% of the fatalities in the world (EM-DAT, 2018). Induced by natural (earthquakes, volcanic eruptions, meteorological events) and anthropogenic triggers (slope modifications, mining, landscape engineering), the increase in

50 the stress of slope materials causes landslides, which can harm numerous elements at risk.
51 Landslides occur heterogeneously in many parts of the world including the Central and South
52 Americas, the Caribbean islands, Asia, Turkey, European Alps, and East Africa (Froude &
53 Petley, 2018). In the past 15 years, we have seen a high number of events that have
54 inadvertently led to the failure of thousands of slopes and causing damage to essential linear
55 infrastructures and population. Some recent examples are Wenchuan, China (2008),
56 Kedarnath, India (2013), Kaikoura, New Zealand (2016), Jiuzhaigou, China (2017), Dominica
57 (2017), Porgera, Papua New Guinea (2018), Hokkaido, Japan (2018), Belluno, Italy (2018),
58 Haiti (2021), Sumatra, Indonesia (2022).

59 These examples indicate that landslide occurrences will probably continue to increase in the
60 short and medium term; therefore, an effective capability of rapid mapping is required to map
61 future event-based landslides. In recent years, state-of-the-art research has been conducted
62 to better understand the impact of natural hazards such as landslides and the cascading
63 effects on the elements-at-risk. A critical understanding of these complex processes begins
64 with the onset of mapping slope failures. This information about the failed slopes is attributed
65 as records and is documented in a "landslide inventory". Landslide inventories include
66 information on the spatial location and extent of the landslides and, if available, also crucial
67 information about 1) the time of occurrence, 2) the triggering event that led slopes to fail, 3)
68 the typology of the landslides based on the accepted standard classifications like (Cruden &
69 Varnes, 1996) and (Hungr et al., 2014), and 4) the volume of the failure. However, regarding
70 rapid mapping of recently occurred landslides, information about the spatial location,
71 distribution, and intersection with affected elements-at-risk are important. , and 4) the volume
72 of the failure. However, regarding rapid mapping of recently occurred landslides, information
73 about the spatial location, distribution, and intersection with affected elements-at-risk are
74 important.

75 When it comes to detecting and mapping landslides over remotely sensed images, it is safe
76 to say that a lot of the current literature in the past couple of years has devised and spent time
77 employing artificial intelligence (AI) models to map landslides automatically, arguably, with
78 good results. These AI models can classify remote sensing images to denote where the
79 landslides are present in the analysed images. However, the core prerequisite for employing
80 AI models is a reliable dataset to be used for training. Recent studies have only focused on
81 mapping landslides with AI but at scales that are small or regional while also claiming that the
82 proposed models can cater towards rapid mapping of landslides at any given time, location
83 and scale (Liu et al., 2022; Meena et al., 2022b; Nava, Bhuyan, et al., 2022; Nava, Monserrat,
84 et al., 2022; Soares et al., 2022a; Tang et al., 2022; Yang et al., 2022; Yang & Xu, 2022).
85 However, seldom has been the case where truly an approach has been taken to map
86 landslides outside the regions where the models are initially trained on, and also towards
87 actually applying the proposed models in capturing and mapping event-based landslides that
88 has recently occurred. Some other works at collectively detecting and mapping landslides of
89 different countries have been attempted by (Prakash et al., 2021) and (Ghorbanzadeh et al.,
90 2022), which showcases the power of employing AI at mapping landslides. Recently, Bhuyan
91 et al. (2023) made some strides at mapping landslides at larger spatiotemporal scales to
92 provide multi-temporal inventories of some famous events but more experiments in to explore
93 other geographical contexts are required. The core of the mentioned studies also heavily relies
94 on the availability of quantity and quality data for training an AI model. The accessibility of
95 such data can 1) allow a model to identify landslides that were caused by different types of
96 triggers (logically leading to the detection of different types of landslides), 2) to map landslides
97 in different parts of the world that vary geomorphologically, and 3) the applicability of the model
98 at mapping newly occurring landslides triggered by events in recent times. The contemporary
99 works of the current literature brings about a critical discussion about the availability and

accessibility of comprehensive and adequate data to effectively train models to detect landslides. Both (Prakash et al., 2021) and (Ghorbanzadeh et al., 2022) have used open-source Sentinel-2 imageries for multi-site landslide detection however, considering the fact that the spatial resolution is 10 metres, a lot of small landslides are missed out or not accurately captured (Meena et al., 2022b). The latter sampled data from 4 different areas/events Sentinel-2 imagery (four bands at 10 meters spatial resolution, six at 20, and three at 60) and combined it with DEM derived data from ALOS-PALSAR. The dataset we propose, instead, is sampled from 10 different areas/events and uses 3 meters spatial resolution imagery. Sampling from more areas can provide a more diverse representation of both landslide and background classes, which can improve the robustness of the model when applied to different regions. Moreover, a dataset with more diversity is likely to generalize better to new unseen data than one with limited diversity, making it more suitable for real-world deployment. Sampling from 10 areas also provides better coverage of the geographical region, reducing the risk of missing important features or patterns. Higher spatial resolution imagery captures more detail, allowing for more accurate identification and segmentation of landslide features. It also allows obtaining a more detailed view, which can be useful to identify small landslides or details that may be difficult to see in lower resolution imagery. Moreover, it can provide more context for the location, helping to better understand the environment and the relationships between different objects and features. Therefore, the increased detail can result in improved accuracy when classifying features and objects, reducing the risk of misclassification.

To effectively and rapidly map landslides after an event, it is required first to determine the spatial extent of the affected areas. Collecting this data is frequently hazardous since it involves individuals on the ground investigating landslides first hand during or immediately after the event. With the increased availability of satellite imagery, this task has the potential to be completed not only remotely but also automatically through the use of powerful deep learning algorithms. Currently, adequate high-resolution satellite imagery of landslides is not widely available. To depict the complex and dynamic nature of the landslides, significant amounts of images must be provided. To this purpose, we present high-resolution global landslide detector database (HR-GLDD), a large-scale satellite image dataset with assembled landslide inventories. The database currently houses 10 geographical areas and 3 recently transpired events (see Figure 1), and we plan to constantly update this database with newer events.

2. Study areas

The study areas were chosen based on the variety of triggering events that resulted in the occurrence of the landslides. Because of the availability of VHR archived Planet Scope imageries after 2016, the most significant landslide events were considered. The geomorphological diversity of the study sites results in a collection of complex landslide phenomenon. We selected the imageries based on the availability of cloud-free conditions in the areas and examined globally archived satellite remote sensing imageries from Planet Scope from the years between 2017 and 2022 (Table 1). We selected 8 study sites across the globe to assemble the database (see figure1). To further test the generalization capabilities of the models trained on the proposed dataset, we choose three recently occurred events: co-seismic landslides in Haiti (August, 2021) and rainfall-induced landslides in Indonesia (February, 2022) and Democratic Republic of Congo (April, 2020) (Meena et al., 2022a).
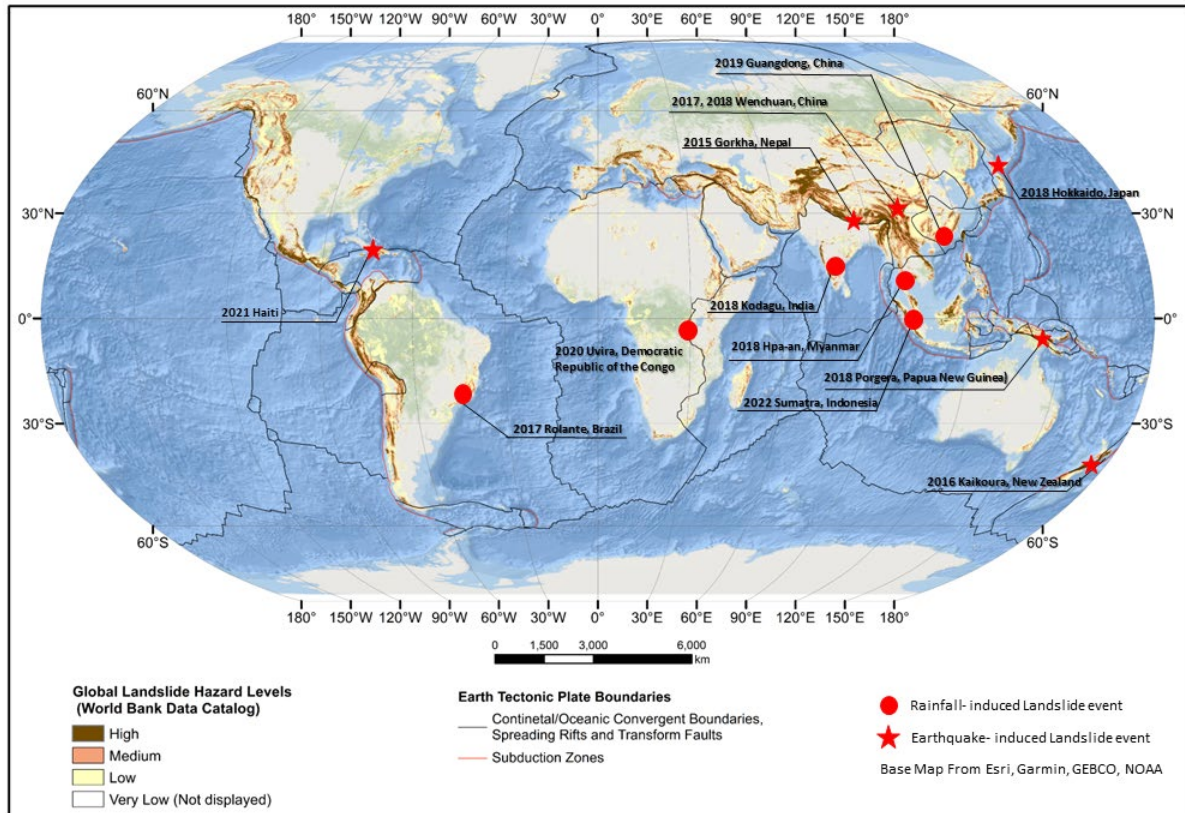
146

147 Figure 1: Collection of rainfall- and earthquake-induced landslide events present in the HR-
148 GLDD.

149

150   2.1. Porgera, Papua New Guinea

151 Papua New Guinea (PNG), located on the Australian continent, is the eastern half of the New
152 Guinea island. This region, characterized by active volcanos, earthquakes, and steep slopes
153 with elevations up to ~4.400 m.a.s.l., is part of the Pacific Ocean's 'Ring of Fire'. The geological
154 and tectonic makeup divides the island into four tectonic belts: Stable platform, Fold Belt,
155 Mobile Belt, and Papuan Fold and Thrust Belt (Tanyaş et al. 2022). Particularly in the east,
156 where PNG lies, there exists an accreted Paleozoic structure known as the Tasman Orogen
157 (Hill and Hall, 2003). Due to these unique geotectonic conditions, the area is frequently
158 affected by landslides associated with the occurrence of earthquakes (Tanyaş et al. 2022). On
159 February 25, 2018, a severe earthquake struck the southern region of the Papuan Fold and
160 Thrust belt (central highlands of PNG), reaching a magnitude of Mw 7.5. This event, the
161 highest magnitude in the region in the past century (Wang et al. 2020), caused significant
162 damage to buildings and energy structures while also triggering a massive number of
163 landslides. This 2018 earthquake in PNG instigated over 200 landslides across the affected
164 area, resulting in numerous fatalities and substantial infrastructural damage. The primary
165 causes for these landslides were the intense ground shaking and the region's steep
166 topography. Additional influential factors included soil characteristics, rainfall, and vegetation
167 cover. A deep understanding of these contributing elements can significantly enhance
168 landslide hazard assessments and aid in reducing future risk (Dang et al., 2020; Xu et al.,
169 2020). Characteristics of the landslides included high relief, steep slopes, and weak lithology.
170 An impressive number of 11,600 landslide scars were recorded post-event, with more than
171 half surpassing an area of 50,000 m² (Tanyaş et al. 2022). Given these realities, effective

174 ### 2.2. Kodagu, India

175 Kodagu district is located in the Karnataka state, Western Ghats, India. The area is
176 characterized by elevations approximately between 50 and 1.750 m a.s.l., metamorphic rocks
177 (e.g., amphibolite, gneiss, and schist), steep slopes, high annual precipitation of about 4000
178 mm, and the presence of croplands (e.g., coffee, rice, and spices) (Jennifer and Saravan,
179 2020; Meena et al. 2021). In August 2018, a rainfall-induced high magnitude mass movement
180 event occurred in Kodagu, the primary landslide type triggered was debris flow (Meena et al.
181 2021). A total of 343 landslides were recorded, including mudflows, rock falls, and debris flows
182 (Meena et al. 2021). The event resulted in several damages to land resources, properties, and
183 loss of human lives (Martha et al. 2018; Jennifer and Saravan, 2020).

184 ### 2.3. Rolante, Brazil

185 The Rolante river catchment study area is located in the Rio Grande do Sul state, southern
186 Brazil. The region being part of the Serra Geral geomorphological unit, has elevations up to
187 ~1.000 m.a.s.l. (Uehara et al. 2020). Moreover, is characterized by the presence of basaltic
188 rocks and sandstones, and annual precipitation thresholds between 1700 and 2000 mm
189 (Uehara et al. 2020, Soares et al. 2022). On 5 January 2017, a high magnitude rainfall-induced
190 mass movement event was triggered, and 308 landslides were registered (Gameiro et al.
191 2019; Quevedo et al. 2019), resulting in several damages to the Rolante municipality.

192 ### 2.4. Tiburon Peninsula, Haiti

193 The Tiburon Peninsula study area is located in the western part of the Hispaniola island (Haiti)
194 with elevation up to 2300 m. a.s.l. Tiburon Peninsula, mainly consists of volcanic rocks such
195 as basalts and sedimentary rocks, namely limestones (Harp et al., 2016). The annual
196 precipitation of the area is more than 1600 mm (Alpert, 1942; USAID, 2014). On 14 August
197 2021, Tiburon Peninsula was struck by a Mw 7.2 earthquake, which was followed by several
198 aftershocks. The strongest one (Mw 5.7) occurred on 15 August 2021. Two days after the
199 mainshock the area was hit by the intense Tropical Cyclone Grace. The combination of the
200 two events triggered thousands of landslides (Martinez et al., 2021) in the Pic Macaya National
201 Park located in western part of the peninsula.

202 ### 2.5. Rasuwa, Nepal

203 The study area is located in the Rasuwa district (central Nepal) in the higher Himalayas with
204 altitudes ranging from 904 to 3267 m. a.s.l and annual average precipitation of 1800-2000 mm
205 (Karki et al., 2016),The geology includes Proterozoic metamorphic rocks such as amphibolite,
206 gneiss, and schist (Tiwari et al., 2017). The area was struck by the Mw 7.8 Gorkha earthquake
207 on 25 April 2015. The intense seismic sequence produced at least 25,000 landslides (Roback
208 et al., 2018).

209 ### 2.6. Hokkaido, Japan

210 The Hokkaido study area is in northern Japan and has a high presence of croplands. The area
211 is characterized by elevations between 50 and 500 m a.s.l., the geology is composed of
212 Neogene sedimentary rocks, formed by the accumulation of numerous layers formed by
213 materials ejected by the Tarumai volcano from several events over the years (Yamagishi and
214 Yamazaki, 2018; Zhao et al. 2020; Koi et al. 2022). A severe earthquake hit the Hokkaido
215 Iburi-Tobu area in Japan on September 6th, 2018. The earthquake registered a magnitude of
216 6.7 according to the Japan Meteorological Agency (JMA) and its epicenter was at 42.72° North

and 142.0° East (Yamagishi and Yamazaki, 2018), located along the southern frontier of Hokkaido. The event triggered thousands of landslides (~7059) in a concentrated area of 466 km² (Zhao et al. 2020) and was responsible for 36 deaths (Yamagishi and Yamazaki, 2018).

2.7. Wenchuan, China

The study area is in the Longmenshan region at the eastern margin of the Tibetan Plateau, China. The location is characterized by high elevations up to 7.500 m a.s.l., the geology consists of lithological units from the Mesozoic, Jurassic, Cretaceous, Paleozoic, Precambrian formations and three types of Quaternary sedimentary units (Qi et al. 2010; Gorum et al. 2011). The area is constantly affected by earthquake-induced landslides over the years (e.g., 2017, 2018, 2019, 2021). The 2008 Wenchuan event is one of the most destructive events of mass movements related to earthquakes in the region (Fan et al. 2018). The Wenchuan earthquake hit a magnitude of Mw 7.9. It was responsible for triggering nearly 200.000 landslides (Xu et al. 2014), besides missing, injured, and thousands of human fatalities in a total area of 31,686.12 km² (Qi et al. 2010).

2.8. Sumatra, Indonesia

The investigated area is Mount Talamau (2912 m) which is a compound volcano located in West Pasaman Regency, West Sumatra Province, Indonesia. Geologically, the volcano consists of andesite and basalt rocks belonging to Pleistocene-Holocene age (Fadhilah & Prabowo, 2020; Zulkarnain, 2016). The climate of the area is humid and tropical and the mean annual precipitation in West Pasaman area is between 3500 and 4500 mm/year (Wilis, 2019). The Mw 6.1 earthquake hit West Sumatra on 25 February 2022. This event triggered several landslides in an area of 6 km^2, along the eastern and north-eastern flank of Talamau volcano.

2.9. Longchuan, China

The study area is located in the vicinity of Mibei village in Longchuan County, Guangdong Province, China with elevations between 180 and 600 m. The area has a subtropical monsoon climate, affected by frequent typhoons and rainstorms from May to October. The average annual precipitation ranges from 1300 to 2500 mm (Bai et al., 2021). The area is composed of Paleozoic completely weathered granite and Quaternary granite residual soil (Bai et al., 2021). Between 10 and 13 June 2019, an intense rainfall event, which was characterized by cumulative rainfall of 270 mm, triggered 327 shallow landslides between 300 and 400 m of altitudes and slopes ranging from 35 to 45° (Feng et al., 2022).

2.10. Hpa-An, Myanmar

The study area is located in Hpa-An district (central Kayin State, South Myanmar) in a tropical and monsoon area with a mean annual precipitation between 4500 and 5000 mm (Win Zin & Rutten, 2017) and elevations up to 1300 meters. The area is part of the Shan Plateau sequence, which includes low grade metamorphosed Precambian, Palezoic and Mesozoic sedimentary rocks (Jain & Banerjee, 2020). On 28–30 July 2018, Myanmar was hit by an extreme rainfall event which caused a flood along Bago river basin and triggered 992 landslides only in Kayin State (Amatya et al., 2022).

2.11. Kaikoura, New Zealand

The 2016 Kaikoura earthquake triggered more than 10,000 landslides in New Zealand, causing extensive damage and disrupting transportation routes. The landslides were complex and involved multiple failure mechanisms, including rockfalls, rock avalanches, and debris flows. The intense shaking and steep topography of the region contributed to the landslides. To reduce the potential impact of future earthquakes, it is crucial to improve understanding of

262 landslide mechanisms and develop effective early warning systems (Goda et al., 2020;
263 Massey et al., 2020; Wang et al., 2020).

2.12. Uvira, Democratic Republic of Congo

265 The city of Uvira in the Democratic Republic of Congo experienced devastating landslides in
266 2020 due to heavy rainfall, poor land management practices, and the steep topography of the
267 region. These landslides caused significant damage to infrastructure and displaced thousands
268 of people. Landslides are a recurring hazard in the DRC, with an average of 100 occurring
269 annually, and climate change is expected to exacerbate the problem. Efforts to mitigate the
270 risk of landslides can include improved land use practices, early warning systems, and
271 infrastructure designed to withstand landslides. Taking a comprehensive approach is key to
272 minimizing the impact of landslides and protecting at-risk communities. (Mwene-Mbeja et al.,
273 2020; Kervyn et al., 2020; United Nations Office for Disaster Risk Reduction, 2020)

3. High-Resolution Global landslide Detector Database (HR-GLDD)

3.1. Data set description:

277 The dataset created in this study consists of images acquired from the PlanetScope satellites
278 (see table 1) and landslide inventories collected from the literature. For all the events,
279 landslides were manually delineated due to unavailability of existing inventories at high
280 reolution. PlanetScope is a constellation of approximately 130 satellites that acquire images
281 of the Earth daily with 3 meters of spatial resolution. The sensors acquire the images with 8
282 spectral bands: coastal blue (431 - 552 nm), blue (465 - 515 nm), green (547 - 583 nm), yellow
283 (600 - 620 nm), red (650 - 680 nm), red-edge (697 - 713 nm) and NIR (845 - 885 nm) (Planet
284 Team, 2019). PlanetScope imagery consists of surface reflectance values and 16 bits images.
285 The images from both sensors are orthorectified and radiometrically corrected by the providers
286 and we undertook the intrasensor harmonization process for the red, green, blue, and NIR
287 bands that is offered by PlanetScope.

288 The dataset was prepared using only the red, green, blue, and NIR bands. The pre-processing
289 phase was based on three steps: generation of binary masks, data sampling, and tiles
290 patching (Meena et al., 2022a).. We used manual image interpretation to manually delineate
291 landslide polygons. First, the interpreted landslides polygons from each area were rasterized
292 using the Rasterio Python library into a binary mask, where "1" represents the landslides and
293 "0" the background. The satellite imagery, along with the mask was then sampled and patched
294 into a regular grid that yields patches of dimension 128 x 128 pixels, which correspond to 14.7
295 km^2 per patch. Since the imbalance between background area and landslides is strong, the
296 images that did not have any landslides pixel labelled were removed. The proportions for the
297 positive samples of landslides against the non-landslides are 9.96% and 90.04%, respectively.
298 Table 1 shows the number of tiles created for each area.

300 Table 1 - Number of tiles, satellite information and landslide statistics for each study area.

Study Area	Satellite	Number of tiles	Study Area in km^2	Number of landslides	Minimum Landslide area (m^2)	Maximum Landslide area (m^2)	Total Landslide area (km^2)
Kodagu (India), 2018	PlanetScope	530	4033.62	343	276.23	581342.19	5.67

Rolante (Brazil), 2017	PlanetScope	33	24.62	113	381.76	81277.53	0.67
Tiburon Peninsula, (Haiti) 2021	PlanetScope	461	130.85	1394	200.74	473696	8.24
Rasuwa (Nepal), 2017	PlanetScope	222	114.68	184	676.85	115567.96	2.45
Hokkaido (Japan), 2018	PlanetScope	159	50.17	715	237.76	48524.72	5.29
Wenchuan (China), 2017	PlanetScope	284	58.25	1415	23.78	98467.96	3.19
Wenchuan (China), 2018	PlanetScope	263	58.25	546	110.18	1289210.19	5.54
Sumatra, (Indonesia,) 2022	PlanetScope	403	22.56	584	302.26	6206089.32	9.73
Longchuan, (China,) 2019	PlanetScope	110	32.22	228	235.21	61163.17	0.73
Hpa-An, (Myanmar), 2018	PlanetScope	101	28.38	540	101.23	88044.20	0.97
Porgera, Papua New Guinea, 2018	PlanetScope	725	304.94	491	262.65	259392.71	5.48
Kaikoura, New Zealand, 2016	PlanetScope	287	150.75	246	676.67	165943.82	3.50
Uvira, Democratic Republic of the Congo, 2020	PlanetScope	247	38.64	394	500.25	106094.52	1.61

301

302   3.2. Design of HR-GLDD

The performance evaluation of the study sites was carried out using metrics and trained using five state-of-the-art U-Net like models, showcasing the capability and applicability of the High-Resolution Global Landslide Detector Database (HR-GLDD). We used a total of ten geographically distinct study sites distributed globally, where landslide events were chosen including different triggering mechanisms such as five earthquake-induced and five rainfall-landslides-, we separately divide the patches into 60% for training, 20% for validation, and 20% for testing the model capabilities. All the sets are then mixed to create a unique dataset composed of equal percentages of patches.

We designed three scenarios to train, predict, and evaluate model performances in order to assess the robustness and applicability of the HR-GLDD. Primarily, we evaluate the model performances on the individual test sets (Meena et al., 2022a).. Secondly, we evaluate the performances of the models on the HR-GLDD test set. Moreover, finally, we test on two completely unseen recently occurred landslide events in Haiti 2021 and Indonesia 2022 (see figure 2).
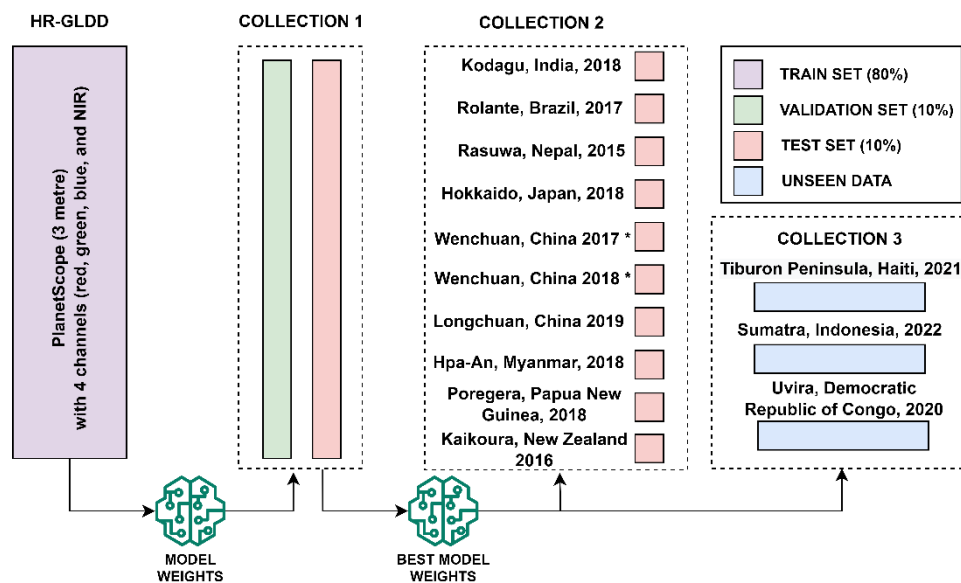
Figure 2: Schematic representation of the division of different components of HR-GLDD. Collection 1 refers to the test and validation data separated from the HR-GLDD. Collection 2 refers to the test dataset of individual sites. Collection 3 refers to the data from three recent events for testing purposes. Please note, while the Wenchuan event transpired in 2008, we've utilized images from a considerably later period, specifically those taken in 2017 and 2018. In an attempt to ensure the precision and accuracy of our analysis, we prioritized images with clearest, minimal cloud coverage.

4. Methodology

4.1. Model Architectures

The proposed dataset is evaluated through several state-of-the-art U-Net like Deep Learning segmentation models. In the past years, the U-Net (Abderrahim et al., 2020) has been used in several landslide detection applications which yield generally the most reliable results (Bhuyan et al., 2022; Meena et al., 2022c; Nava, Bhuyan, et al., 2022). Therefore, we decided to use it as a benchmark model when training on the proposed dataset. Moreover, several improved versions of the same are evaluated. We systematically trained the model using a variety of combinations of the hyper-parameters batch size (8, 16, 32, 64), learning rate (5e-

4, 10e-4, 5e-5, 10e-5) and the number of filters of the first convolutional layer (8, 16, 32, 64). A description of the employed architectures is given in this section.

U-Net: This architecture has been utilized in various semantic segmentation applications, yielding generally outstanding results (Abderrahim et al., 2020). U-Net was employed initially in biomedical picture segmentation (Ronneberger et al., 2015). Low-level representations are captured by a contracting path (encoder), whereas a decoding path captures high-level representations. The encoding path consists of successive convolution blocks and is equivalent to a traditional CNN structure. Two convolutional layers with a 3 x 3 kernel size and a 2 x 2 max-pooling layer are present within every convolutional block. The rectified linear unit (ReLU) activation function is used to activate each convolutional layer (Agarap, 2018). A 2 x 2 max-pooling layer is added to the convolutional block's end in the encoder route to conduct non-linear downsampling, whereas, in the decoder path, a 2 x 2 upsampling layer takes its place. The upsampling layer is positioned right after a 3x3 convolutional layer (see figure S1). We refer to this combination as learnable upconvolution. We refer to this combination as learnable upconvolution.

Residual U-Net (Res U-Net): Res U-Net (Diakogiannis et al., 2020) follows the same U shape as U-Net, whereas here the above-explained convolutional blocks are replaced by residual blocks. This architecture's goal is to improve the learning capacities of the conventional U-Net as well as mitigate the gradient vanishing effect, especially when dealing with deep neural networks (such as U-Net) (see figure S2).

Attention U-Net and Attention Res U-Net: In the conventional U-Net as well as in the Res U-Net, cascading convolutions have been shown to provide false alerts for tiny objects with high form variability (Oktay et al., 2018). To select pertinent spatial information from low-level maps and therefore alleviate the problem, soft attention gates (AGs) are added (see figure S3, S4). The attention gates are built on skip connections, which actively inhibit activations in unnecessary areas, lowering the number of duplicated features (Abraham & Mefraz Khan, 2018).

Attention Deep Supervision Multi-Scale (ADSMS) U-Net: This architecture adopts the Attention U-Net structure, while, in addition, multi-scale image pyramid inputs are fed to the model, and a deep supervision strategy is applied (Abraham & Mefraz Khan, 2018). In practice, multi-scale inputs enable the model to gather that class data, which is more readily available at various sizes. This holds true for both background features and landslides. Lastly, where training data are few and networks are relatively shallow, deep supervision conducts a potent "regularization". More details about the deep supervision strategy used are available in the following section (see figure S5).

4.2. Model training

To train the DL models, we utilized Dice Loss (DL_c) (Eq. 2) (Milletari et al., 2016) as the loss function:

$$DSC_c = \frac{\sum_{i=1}^{N} p_{ic} g_{ic} + \epsilon}{\sum_{i=1}^{N} p_{ic} + g_{ic} + \epsilon} \tag{1}$$

Equation (1) illustrates a two-class Dice score coefficient (DSC) variation for the landslide class c, where $g_{ic} \in \{0,1\}$ and $p_{ic} \in [0,1]$ are the ground truth and predicted labels, respectively. Furthermore, the numerical stability is assured by avoiding division by zero, while N specifies the total number of picture pixels.

$$DL_c = \sum 1 - DSC_c \tag{2}$$

384
385 As an exception, in the ADSMS U-Net model, every high-dimensional feature representation
386 is regulated by Focal Tversky Loss to avoid loss over-suppression, while the final output is
387 controlled by the conventional Tversky Loss (Eq. 4). The focal Tversky loss is a type of loss
388 function that focuses training on challenging cases, specifically those with a Tversky similarity
389 index (TI_c) (Eq. 3) of less than 0.5.

390
$$TI_c = \frac{\sum_{i=1}^{N} p_{ic} g_{ic} + \epsilon}{\sum_{i=1}^{N} p_{ic} g_{ic} + \alpha \sum_{i=1}^{N} p_{i\bar{c}} g_{ic} + \beta \sum_{i=1}^{N} p_{ic} g_{i\bar{c}} + \epsilon} \tag{3}$$

391
392 The Focal Tversky Loss (FTL_c) function incorporates the likelihoods of pixels belonging to the
393 landslide class (p_{ic}) and the background class ($p_{i\bar{c}}$) as well as the corresponding ground truth
394 labels (g_{ic} and $g_{i\bar{c}}$). It is designed to handle significant class imbalances and can be adjusted
395 by modifying the α and β weights to prioritize recall.

396 The FTL_c function is defined as follows:

397
$$FTL_c = \sum_c (1 - TI_c)^{1/\gamma} \tag{4}$$
398
399 where γ ranges between 1 and 3.

400 This deep supervision strategy, described in Lee et al., (2015), requires intermediate layers to
401 be semantically discriminative at all scales. Furthermore, it contributes to ensuring that the
402 attention unit has the power to change responses to a wide variety of visual foreground
403 material. This strategy is adopted from (Abraham & Mefraz Khan, 2018), who propose it along
404 with the ADSMS U-Net architecture. As the loss function optimizer, for all the models, we used
405 a stochastic gradient descent strategy based on an adaptive estimate of first- and second-
406 order moments (Adam), which is useful in problems with uncertain data and sparse gradients
407 (Kingma & Ba, 2015). The precision, recall, F1-score, and Intersection Over Union (IOU)
408 score, the most common accuracy evaluation measures for segmentation models, all of which
409 have been utilized in several landslide detection studies, were used to measure how well the
410 applied DL models performed in detecting landslides. The appropriate combinations of hyper-
411 parameters must be used while training such DL models in order to optimize the model and,
412 therefore, output the best results.

413 ~~To train the DL models, we utilized Dice Loss (Milletari et al., 2016) as the loss function.:~~
414
415 ~~Dice Loss =c1Ni=1picgic+Ni=1pic+gic~~
416
417 ~~Equation (1) illustrates a two-class Dice score coefficient (DSC) variation for class c, where~~
418 ~~gic [0, 1] and pic [0, 1] are the ground truth and predicted labels, respectively. Furthermore,~~
419 ~~the numerical stability is assured by avoiding division by zero, while N specifies the total~~
420 ~~number of picture pixels. As an exception, in the ADSMS U-Net model, every high-dimensional~~
421 ~~feature representation is regulated by Focal Tversky Loss to avoid loss over-suppression,~~
422 ~~while the final output is controlled by the conventional Tversky Loss. This deep supervision~~
423 ~~strategy, described in Lee et al., (2015), requires intermediate layers to be semantically~~
424 ~~discriminative at all scales. Furthermore, it contributes to ensuring that the attention unit has~~
425 ~~the power to change responses to a wide variety of visual foreground material. This strategy~~
426 ~~is adopted from (Abraham & Mefraz Khan, 2018), who propose it along with the ADSMS U-~~
427 ~~Net architecture. As the loss function optimizer, for all the models, we used a stochastic~~
428 ~~gradient descent strategy based on an adaptive estimate of first- and second-order moments~~
429 ~~(Adam), which is useful in problems with uncertain data and sparse gradients (Kingma & Ba,~~
430 ~~2015). The precision, recall, F1-score, and Intersection Over Union (IOU) score, the most~~
431 ~~common accuracy evaluation measures for segmentation models, all of which have been~~

436

437 5. Results

438

439   5.1. HR-GLDD evaluation results

440 The robustness and applicability of the HR-GLDD was tested using the best model weight.
441 We train and calibrate the models using the HR-GLDD. The best weighs for each model are
442 selected based on the model performances on the mixed test set of the HR-GLDD dataset.
443 After running the models on test dataset, batch size of 16 and Adam optimiser with learning
444 rate 5.00E-04 resulted in best model weight. To further evaluate the efficiency and
445 generalization capabilities of the models, we use the model on three unseen datasets to map
446 landslides in the two different geomorphological areas that were recently affected by multiple
447 landslide events. We chose the most recent events one occurred after Uvira, Democratic
448 Republic of Congo (DRC) heavy rainfall event of April 2020. Haiti earthquake in August 2021,
449 one in Sumatra, Indonesia after a heavy rainfall event of February 2022. A total of 247, 461
450 and 403 unseen image patches were evaluated for DRC, Haiti and Indonesia, respectively.

451 Experimental results for landslide detection by utilising the HR-GLDD are presented in Table
452 2. Overall, all the models performed consistently in collections 2 and 3. The F1-score
453 evaluation results for each test case of all the models demonstrate the applicability of the HR-
454 GLDD training dataset for landslide detection results. The average F1-score for HR-GLDD test
455 dataset (collection 1) across all the models was around 0.7045. Furthermore, the same was
456 observed in the individual test sites in collection 2. We also notice that the Precision and
457 Recall are well balanced ranging between 0.6346-0.7661 and 0.6672-0.8121, respectively,
458 indicating stable model predictions. In collection 3, the metrics reveal positive outcomes in
459 terms of mapping the landslides following the respective events, with an average F1-score of
460 0.5562 for DRC, 0.7947 for Haiti and 0.8603 for Indonesia. The recall values are higher than
461 precision values for all the models resulting in average F1-score of 0.7045 (see table 2).
462 Higher values of recall in all models means that the models were able to identify landslide
463 labelled pixels. However due to the use of only the optical bands, the spectral signatures of
464 other similar features (such as riverbeds and flat barren areas) were labelled as landslides
465 which result in false predictions, thereby, accounting for lower precision.

466 In figure 3 we chose a single image patch to showcase the predictions of the various models
467 with respect to the referenced ground truth. Despite the differences in the spectral fingerprints
468 of the satellite images for each study site and the events initiated by an earthquake or rainfall,
469 the models were still capable of recognizing landslide features (see figure 4, 5 and 6).
470 Particularly, we were able to map the recent events in DRC (2020), Haiti (2021) and Indonesia
471 (2022).

472

473

474

475   Table 2: F1 scores of different DL models across sites and HR-GLDD test dataset along
476   with three unseen test sites.

	Study sites	U-NET	Res-U-NET	Attn-U-NET	Attn-res-Unet	ADSMS-U-NET
	Collection 1 (HR-GLDD Test)	**0.7904**	**0.6825**	**0.7446**	**0.6477**	**0.6576**
Collection 2	Kodagu, India, 2018	0.7674	0.6980	0.7628	0.6664	0.6796
	Rolante, Brazil, 2017	0.7739	0.6913	0.6539	0.6830	0.6726
	Rasuwa, Nepal, 2015	0.8972	0.8149	0.8419	0.7695	0.7976
	Hokkaido, Japan, 2018	0.8159	0.7479	0.8124	0.7317	0.7552
	Wenchuan, China, 2017	0.7781	0.6507	0.6981	0.6162	0.6739
	Wenchuan, China, 2018	0.8077	0.6886	0.7295	0.6704	0.6557
	Longchuan, China, 2019	0.6842	0.5076	0.5422	0.4829	0.4398
	Hpa-An, Myanmar, 2018	0.8415	0.7861	0.7826	0.7405	0.7709
	Porgera, Papua New Guinea, 2018	0.7515	0.6150	0.7568	0.6572	0.6261
	Kaikoura, New Zealand, 2016	0.7496	0.5456	0.7335	0.4922	0.6494
	Collection 3					
	Sumatra, Indonesia, 2022	0.8832	0.8810	0.8232	0.8534	0.8608
	Tiburon Peninsula, Haiti, 2021	0.8357	0.8055	0.7869	0.7648	0.7808
	Uvira, Democratic Republic of the Congo, 2020	0.5937	0.5366	0.5682	0.5008	0.5819

477

478
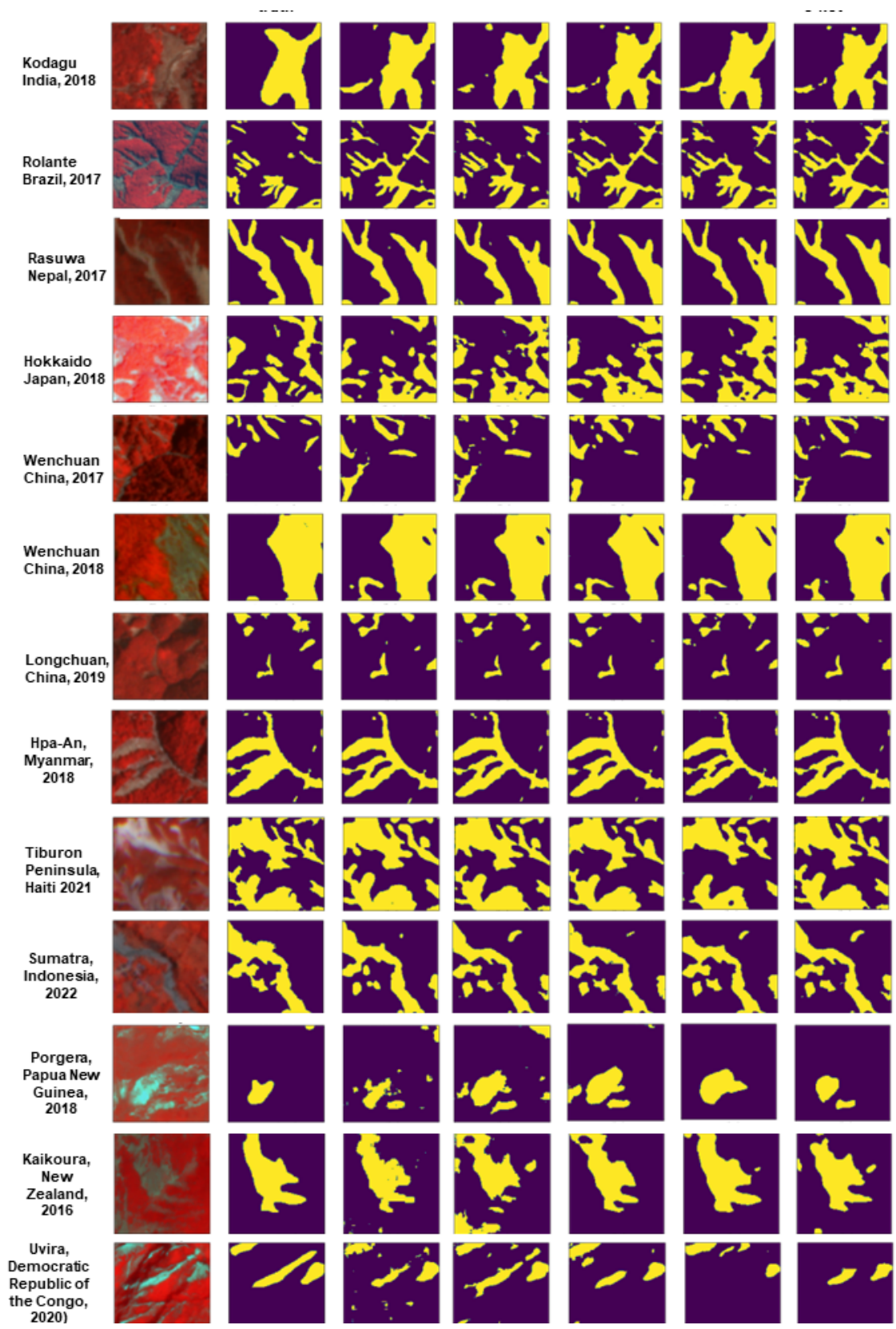
479

480 Figure 3: Landslide predictions made by the different DL models against the ground truth. The
481 base image is shown as a false colour composite (FCC) to better visualize the scars of the
482 landslides.

483
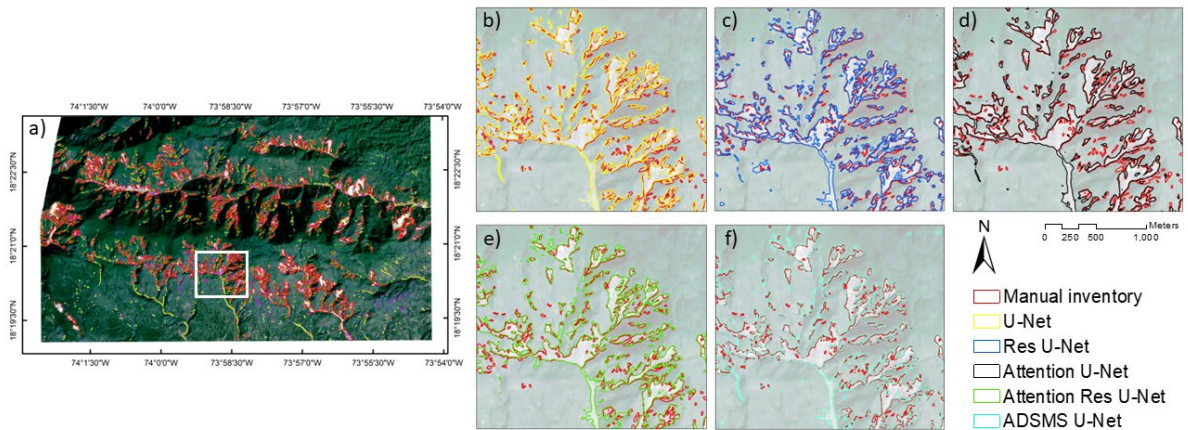
Figure 4: Comparison of ground truth landslides with predictions from the DL models for the unseen dataset of Haiti (We utilized various color coding schemes for the visualization of Deep Learning (DL)-based landslide detection results, allowing for a visual distinction between polygons generated from manual delineation).

488
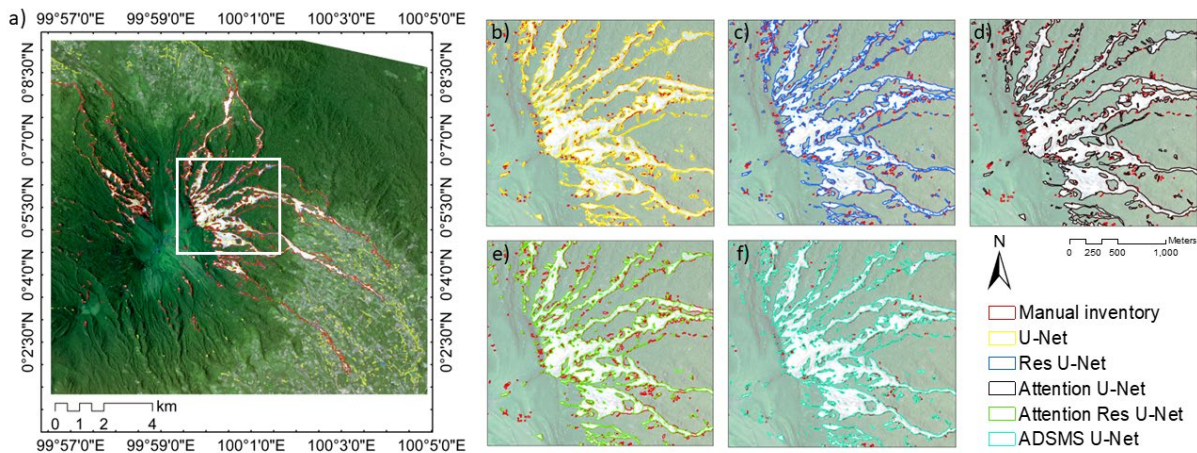
Figure 5: Comparison of ground truth landslides with predictions from the DL models for the unseen dataset of Indonesia Haiti (We utilized various color coding schemes for the visualization of Deep Learning (DL)-based landslide detection results, allowing for a visual distinction between polygons generated from manual delineation).

493
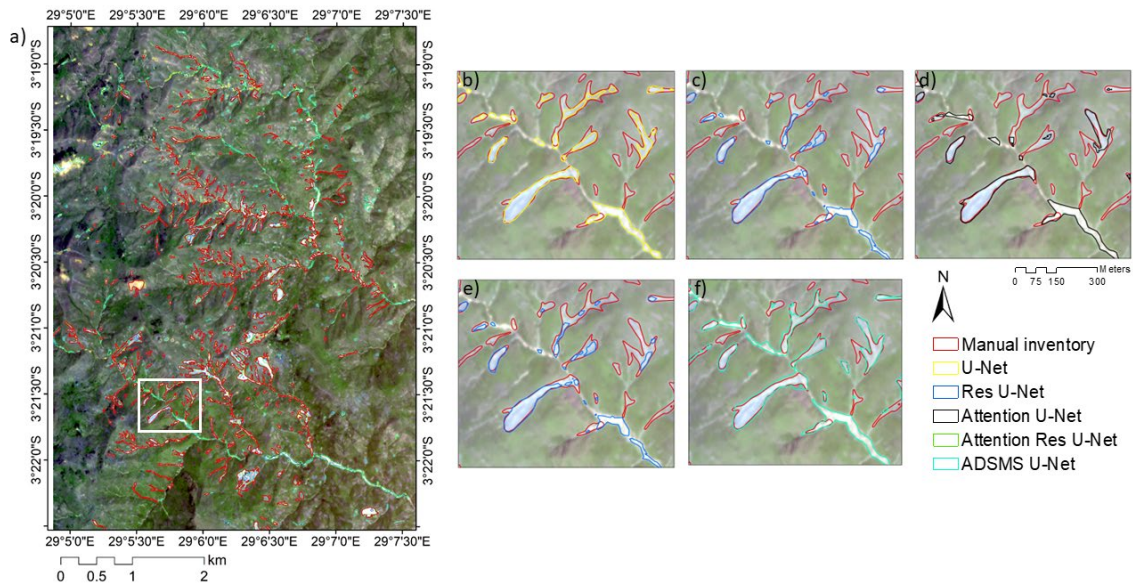
494

495 Figure 6: Comparison of ground truth landslides with predictions from the DL models for the
496 unseen dataset of DRC (We utilized various color coding schemes for the visualization of
497 Deep Learning (DL)-based landslide detection results, allowing for a visual distinction between
498 polygons generated from manual delineation).

499

500 6. Discussions
501 6.1. Advantages of using HR images

502 The spatial resolution of Planet Scope imagery enables the detection of small size landslides
503 that open access satellite missions like Sentinel and Landsat frequently miss due to their
504 spatial and temporal resolution (Meena et al., 2021). Moreover, even though Sentinel-2 has
505 additional spectral bands, the lack of improved spatial resolution inhibits precise boundary
506 delineation and landslide localisation (Meena et al., 2022). The most prominent features of
507 Planet Scope imagery, in addition to its competitive spatial resolution, are its daily temporal
508 resolution and global coverage. Since the satellites have identical sensors, the imageries
509 are orthorectified and image pre-processing are simplified and more accurate. Because
510 Planet imagery provide global coverage, we may extend our study sites to new locations for
511 generating more quality datasets that allow for a better model generalization.

512 6.2. Quality of HR-GLDD

513 The quality of any ML/DL model depends on the data that it is trained on, and the GLDD aims
514 to meet this fundamental requirement. To our knowledge, no other quality data sets exist that
515 can accommodate the wide range of landslide-triggering events and topographical diversity
516 needed for efficient model training. As the GLDD is a strong collection of various landslide
517 events caused both by rainfall and earthquakes. The GLDD is designed to calibrate models
518 able to map new events that will occur in the future. The models investigated in our study gave
519 promising and consistent results for two unseen datasets generated by completely different
520 events, indicating a well-prepared, dependable, and resilient dataset. However, there are clear
521 limitations with the GLDD that must be considered. These problems primarily stem from issues
522 with manually delineated polygons and various uncertainties caused by satellite imagery. A
523 number of different variables, including the mapping scale, the date, and the quality of the
524 satellite imagery, affect how accurate an inventory is. The radiometric resolution and cloud
525 coverage are additional variables that affect the generation of manual inventories. Additionally,

526 haze effect caused by instrument errors hinders model performances. Subjectivity in the
527 landslide polygon boundaries results from the amalgamation problem, which is caused by
528 elements like the investigators' level of experience and the goal of the study.

529   6.3. Significance of the HR-GLDD

530 A thorough hazard and risk framework is made possible by quality landslide inventories
531 however, the generating such inventories at large scales takes ample amount of time and
532 resources. This is where such automatic pipelines can truly shine at creating inventories which
533 can be used for the successive phases of a hazard and risk. Local, regional, and national
534 stakeholders may include such inventories into their risk reduction efforts thanks to the
535 availability of inventories produced automatically. Furthermore, this information may serve as
536 the foundation for a legal framework that implements landslide risk. A landslide risk reduction
537 plan is now more crucial than ever given the anticipated rise in worldwide landslide activity
538 brought on by climate change. Higher landslide activity is expected in the future due to a
539 number of factors, including an increase in the frequency and intensity of seismic events,
540 anthropogenic events, heavy precipitation events, rising ground water levels, storm surges,
541 and a general rise in relative sea level. Therefore, it is essential to comprehend the underlying
542 mechanisms of landslides better and create practical risk reduction techniques to save
543 people's lives and property.

544   6.4. Automated pipeline for HR-GLDD

545 At the moment, automated techniques are the only viable solution for mapping vast regions
546 with accuracy appropriate for operational objectives. Nonetheless, reliable, reproducible, and
547 accurate processes for automating landslide detection across huge data stacks are still
548 absent. As a result, many landslide-affected regions remain unmapped because 1) they are
549 challenging to map using standard methods, and 2) using high-resolution imagery is costly
550 and labour-intensive, with a substantial part of the mapping process dependent on human
551 judgment. By overcoming these challenges, automated pipelines that address these issues
552 can considerably reduce the requirement for human involvement and pave the way for the
553 development of reliable real-time mapping and monitoring of natural hazards at the continental
554 and global scales. Based on the quality of GLDD, reliability of automated pipelines and rapidly
555 growing availability of HR satellite imagery, we can realistically envision mapping of landslide
556 instances and contribute towards generating and updating landslide inventories at large-
557 scales, spatially and potentially, also temporally (Bhuyan et al., 2023).

558 Providing an expert-based, high-quality, and scientifically validated landslide inventory to
559 scientific communities is essential for frameworks of modelling, landslide prediction, machine
560 learning, and deep learning research. The GLDD dataset has been verified, which increases
561 the availability of much-needed training datasets for automated mapping algorithms. The
562 consistently long time taken to compile landslide inventories manually contrasts with the rise
563 in data accessible for landslide mapping. The development of technologies to successfully
564 automate the procedure is the future direction in landslide inventory mapping. The precedence
565 of quality dataset is noted in where they commented that the need for quality datasets will
566 provide a valuable resource for training and developing algorithms.

567 The current dataset is an excellent resource for training and developing future algorithms for
568 this purpose. Automated mapping methods, particularly when combined with publicly available
569 elevation models, can potentially improve our results in future investigations.

570 7. Conclusions

571 Mapping landslides through space is a challenging endeavour. Automated efforts for the same
572 have been explored to some extent, but a transferrable method based on a robust dataset has
573 not yet been investigated. In this paper, we propose a reliable dataset which can be employed
574 by deep learning algorithms to detect new landslides accurately. The predictive capabilities
575 demonstrate the usefulness and application of the dataset to map landslides at large scales.
576 However, the model's predictability must be investigated further in order to identify particular
577 problems to enhance the findings and predictive capabilities for more complicated landscapes.
578 Overall, despite the limitations, the findings are promising, since it is the first time such a HR
579 dataset has been created that caters to a transferable approach of mapping landslides at so
580 many different geomorphological and geographical locations.

581 Data availability

582 The data, working codes and a document with metadata are freely available at
583 https://doi.org/10.5281/zenodo.7189381 and https://github.com/kushanavbhuyan/HR-GLDD-
584 A-Global-Landslide-Mapping-Data-Repository where data in the format of arrays and model
585 configurations in the framework of TensorFlow as can be displayed and used for reproducibility
586 of our results. We also submit the generated landslide inventories in the form of an
587 Environmental Systems Research Institute (ESRI) shapefile. Modules for deep learning can
588 be found at https://www.tensorflow.org/ and original satellite imageries can be found at
589 https://www.planet.com/.

590 Code availability

591 Code used to produce data described in this manuscript, as well as to create figures and
592 tables, can be accessed at https://github.com/kushanavbhuyan/HR-GLDD-A-Global-
593 Landslide-Mapping-Data-Repository

594 Author contribution

595 All the authors contributed to equally to preparation of manuscript from data curation to review
596 of final manuscript.

597 Competing interests

598 The authors declare that they have no conflict of interest.

599 **References**

600 Abderrahim, N. Y. Q., Abderrahim, S., & Rida, A. (2020). Road Segmentation using U-Net
601 architecture. 2020 IEEE International Conference of Moroccan Geomatics (Morgeo), 1–4.
602 https://doi.org/10.1109/Morgeo49228.2020.9121887

603 Abraham, N., & Mefraz Khan, N. (2018). A NOVEL FOCAL TVERSKY LOSS FUNCTION
604 WITH IMPROVED ATTENTION U-NET FOR LESION SEGMENTATION.
605 https://github.com/nabsabraham/focal-tversky-unet

606 Alpert, L. (1942). Rainfall map of Hispaniola. Bulletin of the American Meteorological Society,
607 23, 423–431.

608 Amatya, P., Kirschbaum, D., & Stanley, T. (2022). Rainfall-induced landslide inventories for
609 Lower Mekong based on Planet imagery and semi-automatic mapping method. Geoscience
610 Data Journal, 00, 1–13. https://doi.org/10.1002/gdj3.145

611 Bai, H., Feng, W., Yi, X., Fang, H., Wu, Y., Deng, P., Dai, H., & Hu, R. (2021). Group-occurring
612 landslides and debris flows caused by the continuous heavy rainfall in June 2019 in Mibei

Village, Longchuan County, Guangdong Province, China. Natural Hazards, 108(3), 3181–3201. https://doi.org/10.1007/s11069-021-04819-1

Bhuyan, K., Tanyaş, H., Nava, L. *et al.* Generating multi-temporal landslide inventories through a general deep transfer learning strategy using HR EO data. *Sci Rep* **13**, 162 (2023). https://doi.org/10.1038/s41598-022-27352-y

Bhuyan, K., Meena, S. R., Nava, L., van Westen, C. J., Floris, M., & Catani, F. (2022). Mapping landslides through a temporal lens: An insight towards multi-temporal landslide mapping using the U-Net deep learning model. Earth Arxiv. https://doi.org/https://doi.org/10.31223/X5DM0B

Cruden, D. M., & Varnes, D. (1996). LANDSLIDE TYPES AND PROCESSES. In National Research Council, Transportation Research Board.

Dang, K. T., Wang, G., Su, Y., Xu, Q., & Chen, W. (2020). Landslides triggered by the 2018 M7.5 earthquake in Papua New Guinea. Natural Hazards and Earth System Sciences, 20(6), 1647-1660.

Diakogiannis, F. I., Waldner, F., Caccetta, P., & Wu, C. (2020). ResUNet-a: A deep learning framework for semantic segmentation of remotely sensed data. ISPRS Journal of Photogrammetry and Remote Sensing, 162, 94–114. https://doi.org/10.1016/j.isprsjprs.2020.01.013

EM-DAT. (2018). The emergency events database—Universit´ e catholique de Louvain (UCL)—CRED, D Guha-Sapir.

Fadhilah, & Prabowo, H. (2020). Genes and physical properties of iron sand from Kinali Pasaman. Journal of Physics: Conference Series, 1481(1). https://doi.org/10.1088/1742-6596/1481/1/012015

Fan, X., Scaringi, G., Domènech, G., Yang, F., Guo, X., Dai, L., He, C., Xu, Q., & Huang, R. (2019). Two multi-temporal datasets that track the enhanced landsliding after the 2008 Wenchuan earthquake. Earth System Science Data, 11(1), 35–55. https://doi.org/10.5194/essd-11-35-2019

Feng, W., Bai, H., Lan, B., Wu, Y., Wu, Z., Yan, L., & Ma, X. (2022). Spatial–temporal distribution and failure mechanism of group-occurring landslides in Mibei village, Longchuan County, Guangdong, China. Landslides, May. https://doi.org/10.1007/s10346-022-01904-9

Fred Agarap, A. M. (n.d.). Deep Learning using Rectified Linear Units (ReLU). Retrieved August 15, 2022, from https://github.com/AFAgarap/relu-classifier.

Froude, M. J., & Petley, D. N. (2018). Global fatal landslide occurrence from 2004 to 2016. Natural Hazards and Earth System Sciences, 18(8), 2161–2181. https://doi.org/10.5194/nhess-18-2161-2018

Ghorbanzadeh, O., Xu, Y., Ghamisi, P., Kopp, M., & Kreil, D. (2022). Landslide4Sense: Reference Benchmark Data and Deep Learning Models for Landslide Detection. https://doi.org/10.48550/arxiv.2206.00515

Goda, K., Ren, J., & Anderson, N. (2020). Landslides induced by the 2016 Kaikoura earthquake, New Zealand: characteristics, distribution, and correlations. Landslides, 17(4), 825-839.

Harp, E. L., Jibson, R. W., & Schmitt, R. G. (2016). Map of landslides triggered by the January 12, 2010, Haiti earthquake. https://doi.org/10.3133/sim3353

Hungr, O., Leroueil, S., & Picarelli, L. (2014). The Varnes classification of landslide types, an update. In Landslides (Vol. 11, Issue 2, pp. 167–194). Springer Verlag. https://doi.org/10.1007/s10346-013-0436-y

Jain, A. K., & Banerjee, D. M. (2020). The Indian Subcontinent: Its tectonics. In Proceedings of the Indian National Science Academy (Vol. 86, Issue 1). https://doi.org/10.16943/ptinsa/2020/49834

Karki, R., Talchabhadel, R., Aalto, J., & Baidya, S. K. (2016). New climatic classification of Nepal. Theoretical and Applied Climatology, 125(3–4), 799–808. https://doi.org/10.1007/s00704-015-1549-0

Kervyn, M., Jacobs, L., Sumbwe, J., Maki Mateso, J. C., Kervyn, F., Sebagenzi, S. N., & Havenith, H. B. (2020). Landslide hazard and risk assessment in the Democratic Republic of Congo. Landslides, 17(8), 1901-1916.

Kingma, D. P., & Lei Ba, J. (n.d.). ADAM: A METHOD FOR STOCHASTIC OPTIMIZATION.

Lee, C.-Y., Xie, S., Gallagher, P., Zhang, Z., & Tu, Z. (n.d.). Deeply-Supervised Nets.

Liu, Y. ;, Yao, X. ;, Gu, Z. ;, Zhou, Z. ;, Liu, X. ;, Chen, X. ;, Wei, S., Liu, Y., Yao, X., Gu, Z., Zhou, Z., Liu, X., Chen, X., & Wei, S. (2022). Study of the Automatic Recognition of Landslides by Using InSAR Images and the Improved Mask R-CNN Model in the Eastern Tibet Plateau. Remote Sensing 2022, Vol. 14, Page 3362, 14(14), 3362. https://doi.org/10.3390/RS14143362

Martinez, S. N., Allstadt, K. E., Slaughter, S. L., Schmitt, R. G., Collins, E., Schaefer, L. N., & Ellison, S. (2021). Landslides triggered by the August 14, 2021, magnitude 7.2 Nippes, Haiti, earthquake. Open-File Report.

Massey, C. I., Hancox, G. T., & Van Dissen, R. J. (2020). The 2016 Kaikoura, New Zealand, Earthquake: A Complex Multihazard and Multirisk Event. Annual Review of Earth and Planetary Sciences, 48, 235-259.

Meena, S. R., Ghorbanzadeh, O., van Westen, C. J., Nachappa, T. G., Blaschke, T., Singh, R. P., & Sarkar, R. (2021). Rapid mapping of landslides in the Western Ghats (India) triggered by 2018 extreme monsoon rainfall using a deep learning approach. Landslides, 18(5). https://doi.org/10.1007/s10346-020-01602-4

Meena Sansar Raj, Lorenzo nava, Kushanav Bhuyan, Silvia Puliero, Lucas Pedrosa Soares, Helen Cristina Dias, Mario Floris, & Filippo Catani. (2022a). HR-GLDD: A globally distributed high resolution landslide dataset [Data set]. Zenodo. https://doi.org/10.5281/zenodo.7189381

Meena, S. R., Soares, L. P., Grohmann, C. H., van Westen, C., Bhuyan, K., Singh, R. P., Floris, M., & Catani, F. (2022b). Landslide detection in the Himalayas using machine learning algorithms and U-Net. Landslides, 19(5), 1209–1229. https://doi.org/10.1007/s10346-022-01861-3

Milletari, F., Navab, N., and Ahmadi, S.-A. (2016). V-Net: Fully Convolutional Neural Networks for Volumetric Medical Image Segmentation. In Proceedings of the Fourth International Conference on 3D Vision (3DV), 565-571. doi: 10.1109/3DV.2016.79.

Mwene-Mbeja, M., Mugaruka, J. P., Bisimwa, B., & Tchicaya, L. (2020). Landslide hazard and risk assessment in Uvira city, Democratic Republic of Congo. Environmental Hazards, 19(3), 263-278.

Nava, L., Bhuyan, K., Meena, S. R., Monserrat, O., & Catani, F. (2022). Rapid Mapping of Landslides on SAR Data by Attention U-Net. Remote Sensing 2022, Vol. 14, Page 1449, 14(6), 1449. https://doi.org/10.3390/RS14061449

Nava, L., Monserrat, O., & Catani, F. (2022). Improving Landslide Detection on SAR Data Through Deep Learning. IEEE Geoscience and Remote Sensing Letters, 19. https://doi.org/10.1109/LGRS.2021.3127073

Oktay, O., Schlemper, J., le Folgoc, L., Lee, M., Heinrich, M., Misawa, K., Mori, K., Mcdonagh, S., Hammerla, N. Y., Kainz, B., Glocker, B., & Rueckert, D. (n.d.). Attention U-Net: Learning Where to Look for the Pancreas.

Planet Team. (2019). Planet Imagery Product Specifications August 2019. 97.

Prakash, N., Manconi, A., & Loew, S. (2021). A new strategy to map landslides with a generalized convolutional neural network. Scientific Reports, 11(1), 1–15. https://doi.org/10.1038/s41598-021-89015-8

Roback, K., Clark, M. K., West, A. J., Zekkos, D., Li, G., Gallen, S. F., Chamlagain, D., & Godt, J. W. (2018). The size, distribution, and mobility of landslides caused by the 2015 Mw7.8 Gorkha earthquake, Nepal. Geomorphology, 301, 121–138. https://doi.org/10.1016/j.geomorph.2017.01.030

Ronneberger, O., Fischer, P., & Brox, T. (2015). U-Net: Convolutional Networks for Biomedical Image Segmentation (pp. 234–241). https://doi.org/10.1007/978-3-319-24574-4_28

Soares, L. P., Dias, H. C., Garcia, G. P. B., & Grohmann, C. H. (2022a). Landslide Segmentation with Deep Learning: Evaluating Model Generalization in Rainfall-Induced Landslides in Brazil. Remote Sensing, 14(9), 2237. https://doi.org/10.3390/rs14092237

Tang, X., Tu, Z., Wang, Y., Liu, M., Li, D., & Fan, X. (2022). Automatic Detection of Coseismic Landslides Using a New Transformer Method. Remote Sensing, 14(12), 2884. https://doi.org/10.3390/rs14122884

Tiwari, B., Ajmera, B., & Dhital, S. (2017). Characteristics of moderate- to large-scale landslides triggered by the Mw 7.8 2015 Gorkha earthquake and its aftershocks. Landslides, 14(4), 1297–1318. https://doi.org/10.1007/s10346-016-0789-0

United Nations Office for Disaster Risk Reduction. (2020). Landslide risk reduction in the Great Lakes Region. Retrieved from https://www.undrr.org/publication/landslide-risk-reduction-great-lakes-region

USAID. (2014). Haiti Securite Alimentaire en Bref.

Wang, F., Fan, X., Yunus, A. P., Siva Subramanian, S., Alonso-Rodriguez, A., Dai, L., Xu, Q., & Huang, R. (2019). Coseismic landslides triggered by the 2018 Hokkaido, Japan (Mw 6.6), earthquake: spatial distribution, controlling factors, and possible failure mechanism. Landslides, 16(8), 1551–1566. https://doi.org/10.1007/s10346-019-01187-7

Wang, T., Liu, C., Saito, H., Nishimura, Y., & Wang, G. (2020). Landslide susceptibility mapping following the 2016 Kaikoura earthquake, New Zealand. Landslides, 17(11), 2617-2630.

Wilis, R. (2019). Impact Variability of Rainfall Intensity to Horticulture Productivity at West Pasaman Regency , Province of West Sumatera , Indonesia. Core.Ac.Uk, 7(10), 138–145.

738 Win Zin, W., & Rutten, M. (2017). Long-term Changes in Annual Precipitation and Monsoon
739 Seasonal Characteristics in Myanmar. Hydrology: Current Research, 08(02).
740 https://doi.org/10.4172/2157-7587.1000271

741 Xu, Q., Dang, K. T., Su, Y., Chen, W., & Wang, G. (2020). Characteristics of landslides
742 triggered by the 2018 M7.5 earthquake in Papua New Guinea. Landslides, 17(1), 145-157.

743 Yang, Z., & Xu, C. (2022). Efficient Detection of Earthquake−Triggered Landslides Based on
744 U−Net++: An Example of the 2018 Hokkaido Eastern Iburi (Japan) Mw = 6.6 Earthquake.
745 Remote Sensing, 14(12), 2826. https://doi.org/10.3390/rs14122826

746 Yang, Z., Xu, C., & Li, L. (2022). Landslide Detection Based on ResU-Net with Transformer
747 and CBAM Embedded: Two Examples with Geologically Different Environments. Remote
748 Sensing, 14(12), 2885. https://doi.org/10.3390/rs14122885

749 Zulkarnain, I. (2016). Sumatra is not a homogeneous segment of Gondwana derived continel
750 blocks: A New Sight based on Geochemical Signatures of Pasaman Volcanic in West
751 Sumatera. Jurnal RISET Geologi Dan Pertambangan, 26(1), 1.
752 https://doi.org/10.14203/risetgeotam2016.v26.271

753

754

755